Analytical Approach to the Local Contact Potential Difference on (001) Ionic Surfaces: Implications for Kelvin Probe Force Microscopy

Franck Bocquet, Laurent Nony, Christian Loppacher, Thilo Glatzel

Published in Phys. Rev. B **78**, 035410 (2008)

Analytical Approach to the Local Contact Potential Difference on (001) Ionic Surfaces: Implications for Kelvin Probe Force Microscopy

Franck Bocquet[1,2], Laurent Nony[1,2,*], and Christian Loppacher[1,2]

[(1)] *Aix-Marseille Université, IM2NP,*
Centre Scientifique de Saint-Jérôme,
Avenue Escadrille Normandie-Niemen, Case 151,
F-13397 Marseille CEDEX 20, France

[(2)] *CNRS, IM2NP (UMR 6242), F-13397 Marseille-Toulon, France*

Thilo Glatzel

Department of Physics, University of Basel,
Klingelbergstr. 82, CH-4056 Basel, Switzerland

(Dated: July 9, 2008)

* To whom correspondence should be addressed; E-mail: laurent.nony@im2np.fr.

Abstract

An analytical model of the electrostatic force between the tip of a non-contact Atomic Force Microscope (nc-AFM) and the (001) surface of an ionic crystal is reported. The model is able to account for the atomic contrast of the local contact potential difference (CPD) observed while nc-AFM-based Kelvin Probe Force Microscopy (KPFM) experiments. With the goal in mind to put in evidence this short-range electrostatic force, the Madelung potential arising at the surface of the ionic crystal is primarily derived. The expression of the force which is deduced can be split into two major contributions: the first stands for the coupling between the microscopic structure of the tip apex and the capacitor formed between the tip, the ionic crystal and the counter-electrode; the second term depicts the influence of the Madelung surface potential on the mesoscopic part of the tip, independently from its microscopic structure. The former has the lateral periodicity of the Madelung surface potential whereas the latter only acts as a static component, which shifts the total force. These short-range electrostatic forces are in the range of ten pico-Newtons. Beyond the dielectric properties of the crystal, a major effect which is responsible for the atomic contrast of the KPFM signal is the ionic polarization of the sample due to the influence of the tip/counter-electrode capacitor. When explicitly considering the crystal polarization, an analytical expression of the bias voltage to be applied on the tip to compensate for the local CPD, *i.e.* to cancel the short-range electrostatic force, is derived. The compensated CPD has the lateral periodicity of the Madelung surface potential. However, the strong dependence on the tip geometry, the applied modulation voltage as well as the tip-sample distance, which can even lead to an overestimation of the real surface potential, makes quantitative KPFM measurements of the local CPD extremely difficult.

PACS numbers: 07.79.Lh, 41.20.Cv, 73.40.Cg

Keywords: non-contact Atomic Force Microscopy; Kelvin Probe Force Microscopy; Local Contact Potential Difference; Short-range Electrostatic Force; Analytical model; Madelung Surface Potential; Ionic crystal

I. INTRODUCTION

Electrostatic forces play a key role in non-contact Atomic Force Microscopy (nc-AFM), not only in the imaging process[1] but also for the investigation of the surface electronic properties. Electronic properties such as the work function and surface charges can be acquired by Kelvin Probe Force Microscopy (KPFM)[2,3] simultaneously to imaging topography by nc-AFM. In KPFM, a feedback is used to apply a voltage between the tip and the sample in order to minimize the electrostatic tip-sample interaction. For metals, this voltage is equal to the contact potential difference (CPD), *i.e.* the bias voltage to be applied between the tip and the surface to align their fermi levels. It is connected to the difference between the work functions of the two surfaces, and thereby to their local electronic properties, according to:

$$\Delta\phi = \phi_{tip} - \phi_{sample} = qV_{cpd}, \tag{1}$$

q being the elementary electrical charge: $q = 1.6 \times 10^{-19}$ C.

Nowadays, two KPFM-based techniques provide facilities to map the spatial variations of the CPD on the nanometer scale, namely Frequency-[4] or Amplitude-Modulation-KPFM[5,6,7] (FM- or AM-KPFM, respectively). These methods were primarily applied to metallic and semiconducting surfaces to study the distribution of dopants in semiconductors[8], or the adsorption of organic molecules (for an overview see ref.[9]). In a few experiments, even molecular[10] or atomic[11,12,13] contrast has been reported. The extension of the technique to insulating surfaces, was performed more recently, as demonstrated by the results reported on thin ionic films on metals[14,15], or on the contribution of bulk defects to the surface charge state of ionic crystals[16,17].

In this work, atomic corrugation of the CPD signal is reported for the first time on the (001) surface of a bulk ionic crystal of KBr. For that purpose, KPFM experiments were carried out in ultrahigh vacuum with a base pressure below 10^{-10} mbar using a home built non-contact atomic force microscope operated at room temperature[18]. A highly doped silicon cantilever with a resonance frequency $f_0 \approx 160$ kHz, and a spring constant $k \approx 21$ N.m^{-1} was used. The typical oscillation amplitude of the fundamental bending resonance was ≈ 10 nm. The cantilever was annealed (30 min @ 120°) and gently sputtered with Ar^+ ions (1-2 min @ 680 eV). The KBr crystal was cleaved in ultrahigh vacuum along the (001)-plane and subsequently annealed at 120° during an hour. The KPFM signal was detected using the

AM mode, as described in detail in Ref. 5. While these experiments, atomic-scale contrast was as well visible in the topography channel (data not shown). The CPD measurements are reported in figs.1a and b. In fig.1a, the image exhibits atomic features, the measured period of which is 0.63 nm, which is visible in the joint cross section. This value matches to a good agreement the lattice constant of KBr, 0.66 nm. The vertical contrast yields about 100 mV around an average value of -3.9 V, the origin of which will be discussed in section IV B. A striking aspect of those results is the robustness of the imaging process in terms of stability and reproducibility upon the tips used. These results suggest an intrinsic imaging process relying on the microscopic origin of the contact potential arising at the sample surface. In this case, the CPD rather turns into *local CPD*, consistently with the concept of *local work function* which has been introduced by Wandelt on metals[19]. By "intrinsic imaging process", it is meant that the contrast can be accounted for with a tip consisting of a single material, namely a metal. Thus, the atomic contrast neither relies on adsorbed nor on unstable species at the tip apex, as often reported for topographic[20] or dissipation[21] imaging by nc-AFM.

In this work, in order to understand the local CPD contrast formation, an electrostatic model is proposed that allows us to derive an expression of the short-range electrostatic force occurring between a biased metallic tip of a nc-AFM microscope and the surface of a bulk dielectric. On the contrary to more refined numerical methods proposed in the literature for almost similar systems[22,23], the analytical development is restricted to a simple tip geometry and a classical, continuous electrostatic approach. Notwithstanding, the model allows us to define a general frame, able to put in relation the surface electrostatic properties with the imaging process yielding atomic contrast of the CPD on ionic surfaces. Obviously, the main results presented here remain qualitatively correct for more complex tip geometries, although numerical methods are then required to get quantitative numbers.

The motivations for that work are twofold. On the one hand, to our knowledge, a compact modelization of the short-range electrostatic forces responsible for the atomic contrast in KPFM on a bulk ionic crystal is still lacking. On the other hand, when evaluating KPFM experiments, the relative complexity of FM- or AM-KPFM experimental setups, both including four electronic controllers, makes the interpretation of the experimental images, and primarily CPD images, tedious, especially when dealing with atomic resolution. Several groups analyzed the KPFM imaging mechanism in order to evaluate their data in terms of quantitative values and lateral resolution[24,25,26,27,28,29,30,31,32,33], a few of them also compared

AM- and FM-KPFM in terms of evaluating the force and its gradient, respectively[7,31]. The fact that many of the above mentioned calculations point out that KPFM results, especially for nano-objects, show a strong distance dependence, clearly points out that for a careful analysis, it is not sufficient to only calculate the electrostatic tip-sample interaction. It is rather important to perform simulations including all imaging mechanisms and in particular also the distance control in order to exclude artifacts due to the feedback circuits. In order to explore the origin of the CPD atomic contrast, we are aiming to closely mimic a real KPFM setup by means of an earlier developed nc-AFM simulator[34]. In the present case of an ionic surface, it is required to consider a large slab of ions, virtually infinite, to describe properly the electrostatic interaction. This is hardly feasible by means of *ab initio* calculations which fail to describe tip-surface systems involving a too big number of atoms. Therefore, prior to simulating the CPD contrast on ionic surfaces by means of our simulator, which is the scope of a future work, we have to find an analytical expression for the electrostatic tip-sample interaction.

The following section details the boundary-value electrostatic problem leading to the expression of the force (section III). In section IV, the analytical expression of the local CPD is derived and discussed to be put in relation with the experimental observations. The implications for KPFM experiments are discussed as well.

II. ELECTROSTATIC MODEL

The geometry of the problem of FM- or AM-KPFM experiments applied to bulk insulating materials is reported in fig.2b. The dielectric sample is an alkali halide crystal like NaCl, KBr, KCl with a fcc structure and a lattice constant a (*cf.* fig.2a). In the area where the tip is, the model assumes that the crystal carries neither net charge, nor local dipole. Its thickness h_d is much larger than all other distances of the problem, typically a few millimeters. Below the surface, the crystal is treated as a continuous dielectric medium with a dielectric permittivity ϵ_d. At the surface, the atomic corrugation of the crystal is described by a single layer of alternate point charges arranged with a fcc structure perpendicular to the [001] direction. The layer extends infinitely in the plane direction. The motivation for such a rationalization of the problem will be justified in section (II B).

The crystal lies on a metallic sample holder (hereafter referred to as the counter-

electrode), with respect to which the tip is biased. The counter-electrode is a planar and perfect conductor. The tip is also assumed to be a perfect conductor which is biased at V_b. In order to preserve the analyticity of the model, the electrostatic boundary-value problem is restricted to a tip with a very simple apex geometry, namely: a hemispherical mesoscopic part (radius $R \simeq 5$ nm) on top of which is half-embedded a small spherical asperity (radius $R_a \ll R$). The contributions of the cantilever and of the macroscopic part of the tip to which the apex is connected to are assumed to be negligible. This issue will be justified in section III A. The tip-surface distance is denoted z_μ (typically a few Å).

The electric field $\overrightarrow{E}$ produced locally between the tip, the dielectric, and the counter-electrode polarizes the ionic crystal, which acquires a macroscopic polarization $\overrightarrow{P} = n_v \overrightarrow{p_l}$ oriented along $\overrightarrow{E}$. In the former equation, n_v is the number of polarizable species *per* unit volume and $\overrightarrow{p_l}$, the local dipolar moment *per* unit cell. In KPFM, the bias voltage V_b is modulated at frequencies which do not influence the electronic polarization of the ions. The major part of the crystal polarization has rather an ionic character, *i.e.* a net displacement in opposite directions of the ions due to their charge $\pm q$ with respect to their equilibrium positions, $\pm\delta/2$, with $\delta = p_l/q$, q being the elementary electrical charge. The polarization effect occurs as well at the crystal surface, where the positions of the ions become modulated perpendicularly to the surface plane, *i.e.* $\delta \rightarrow \delta^\perp$, as sketched in figs.2b and d. $\delta^\perp$ is proportional to the local electric field $\overrightarrow{E_l}$ at any ionic site and to the total polarizability of the dielectric restricted, in our approach, to the ionic polarizability α_i (ref.[35]). Usually, $\overrightarrow{E_l}$ differs from the external electric field $\overrightarrow{E}$ due to the biased tip because $\overrightarrow{E_l}$ explicitly depends on the polarization of the dielectric. The Lorentz's model links $\overrightarrow{E_l}$ and $\overrightarrow{E}$ (ref.[36]), thus, $\overrightarrow{p_l}$ is written:

$$\overrightarrow{p_l} = \alpha_i \epsilon_0 \overrightarrow{E_l} = \chi_d \overrightarrow{E} = q\delta^\perp \frac{\overrightarrow{E}}{E}, \tag{2}$$

with $\chi_d = \alpha_i\epsilon_0/(1 - n_v\alpha_i/3)$, the dielectric susceptibility of the sample. In the former equation, it is important to notice that $\overrightarrow{p_l}$ depends on $\overrightarrow{E}$ and hence on the bias voltage V_b. Consequently, this is also true for $\delta^\perp$. For the sake of discussions, the bias dependence will henceforth be explicitly outlined $\delta^\perp \rightarrow \delta^\perp(V_b)$. Despite $\delta^\perp(V_b)$ cannot be estimated at this point, it is crucial to keep in mind that the sample surface is polarized by the influence of the bias since this is a key aspect of the origin of the CPD atomic contrast.

Our approach of the electrostatic boundary-value problem relies on an *ad hoc* assumption.

The tip, being a perfect conductor, develops a surface charge density σ, the origin of which is split into two main contributions $\sigma = \sigma_m + \sigma_\mu$, namely:

- a charge density σ_m due to the capacitor formed between the biased tip and the counter-electrode with the dielectric in between (*cf.* fig.2c). Owing to the distance between the electrodes, *i.e.* roughly the dielectric thickness h_d, σ_m has a mesoscopic character. It is not influenced by the local structure of the tip apex, but rather by its overall shape.

- a charge density σ_μ originating from the Madelung potential that expands at the crystal surface. When the tip is at a distance z_μ where the potential is effective, typically a few Ångströms, then it develops, in addition to σ_m, a surface charge density σ_μ (*cf.* fig.2d). σ_μ has a microscopic character and must strongly depend on the local structure of the tip apex and on z_μ.

Despite the simple tip geometry that has been assumed, the calculation of the electrostatic force acting on it due to the combined influence of the capacitive coupling and of the Madelung surface potential has no exact analytical solution. Nevertheless, one can build up an approximate solution to the boundary-value problem relying on the superposition principle. For that purpose, the problem is split up into two boundary-value sub-problems schemed in figs.2c and d:

- problem *A*: the tip biased at V_b in front of a dielectric continuous medium (height h_d, dielectric permittivity ϵ_d) held on an infinite planar conductor, the counter-electrode (fig.2c). The local structure of the dielectric is not supposed to influence the tip. This is the description of the "capacitive" problem, the solution of which provides the surface charge density σ_m.

- problem *B*: the tip now biased at 0 V with an infinite plane of alternate point charges located at the same distance than the surface of the dielectric in problem A, *i.e.* z_μ. The layer of point charges is polarized under the electric field that occurs in problem A (fig.2d). This describes the "microscopic" problem. The solution provides the surface charge density σ_μ.

Besides, in order to carry out the calculations more easily, it is convenient to distinguish the two following geometrical areas on the tip (*cf.* fig.2d), namely: the asperity, area (1), *i.e.*

a half-sphere with radius R_a and the mesoscopic tip apex around it, area (2), a sphere with radius $R \gg R_a$ (typically $R/R_a \geq 50$). These two areas do not overlap, but the continuity between them is ensured. The vertical force acting on the tip[37] is written in terms of σ_m and σ_μ as described above:

$$F = \int_{\text{tip}} \frac{(\sigma_m + \sigma_\mu)^2}{2\epsilon_0} \widehat{n}.\widehat{u}_z d\mathcal{S} = F_m + F_{m\mu} + F_\mu \tag{3}$$

$\widehat{n}$ and $\widehat{u}_z$ are the normal to the tip surface and the unitary vector along the vertical z axis of the problem, respectively. Doing so, we only focus on the vertical resultant of the force acting onto the tip. The above expression can be expanded into three components: a purely capacitive part, F_m originating from the tip/dielectric/counter-electrode capacitor; a coupling part, $F_{m\mu}$, which can be interpreted in terms of the resulting force of all the elementary forces due to the electric field σ_m/ϵ_0 onto each elementary charge $\sigma_\mu d\mathcal{S}$ produced on the tip by the influence of the Madelung potential of the crystal, V_s; and a purely microscopic part, F_μ, standing for the short-range electrostatic force due to V_s.

A. Problem A: estimation of σ_m

Although the boundary-value problem of a planar conductor biased with respect to another one with an incomplete dielectric layer in between yields an expression of the surface charge density, the problem with the sphere does not. However, one can argue that the expression of σ_m must be a combination between a configuration in which there is no dielectric medium in the sphere/counter-electrode interface and an opposite one, where the interface is completely filled with it. One can therefore postulate an effective dielectric permittivity $\widetilde{\epsilon}_d = K\epsilon_d$, where K (< 1) is a constant to be set. Owing to the fact that the mesoscopic part of the tip apex, referred to as area (2), is located at a distance $z_m = z_\mu + h_d \gg R$ from the counter-electrode, the analytical expression of $\sigma_m^{(2)}$, explicitly calculated in refs.[37,38], asymptotically trends towards the surface charge density of an isolated, biased sphere[37]:

$$\sigma_m^{(2)} \overset{z_m \gg R}{=} \frac{\widetilde{\epsilon}_d \epsilon_0 V_b}{R} \tag{4}$$

To get the surface charge density on area (1), $\sigma_m^{(1)}$, we seek the potential $V_m^{(1)}$ which equals V_b over the asperity. For that purpose, a spherical coordinate system (r, θ, φ) centered on

the asperity is chosen. The problem having an azimuthal symmetry, the sought potential can be expanded in Legendre polynomials[37]:

$$V_m^{(1)}(r,\theta) = \sum_{n=0}^{\infty} \left(\alpha_n r^n + \frac{\beta_n}{r^{n+1}} \right) P_n(\cos\theta) \tag{5}$$

At large distance from the asperity, $r \gg R_a$, the potential must be similar to the one of a sphere with radius R biased at V_b, namely[37]:

$$V_m^{(1)}(r,\theta) \overset{R>r\gg R_a}{=} V_b \sum_{n=0}^{\infty} \left(\frac{r}{R} \right)^n P_n(\cos\theta) \tag{6}$$

Hence, the coefficients α_n of the expansion are known. The coefficients β_n are deduced from the property of orthogonality of the Legendre polynomials at the boundary condition $V(r = R_a) = V_b$. The potential is finally written:

$$V_m^{(1)}(r,\theta) = V_b \left\{ 1 + \sum_{n=1}^{\infty} \left[\left(\frac{r}{R} \right)^n - \frac{R_a^{2n+1}}{R^n r^{n+1}} \right] P_n(\cos\theta) \right\} \tag{7}$$

The former equation rigorously describes the potential of a system apex/asperity where the junction point between the two spheres is smoothed and not singular, as sketched in fig.2d. Nevertheless, for $R \gg R_a$, the influence of the singular area is negligible. Therefore, equ.7 is a good approximation to the boundary-value problem. The normal derivation along the surface of the asperity yields the expression of $\sigma_m^{(1)}$:

$$\sigma_m^{(1)} = -\frac{\widetilde{\epsilon}_d \epsilon_0 V_b}{R} \sum_{n=1}^{\infty} (2n+1) \left(\frac{R_a}{R} \right)^{n-1} P_n(\cos\theta) \tag{8}$$

Owing to the condition $R \gg R_a$, the sum can be restricted to the first term. Therefore:

$$\sigma_m^{(1)} = -\frac{3\widetilde{\epsilon}_d \epsilon_0 V_b}{R} \cos\theta \tag{9}$$

Thus, despite $\sigma_m^{(1)}$ develops on the asperity, its strength is governed by the radius of the mesoscopic part of the tip apex, R and not by the local radius of curvature of the asperity, R_a.

B. Problem B: estimation of σ_μ

The calculation of the surface charge density σ_μ on the mesoscopic sphere+asperity is more tedious, primarily because it relies on the estimation of the Madelung potential of the ionic crystal, V_s. The boundary-value problem is now restricted to the determination of the surface charge density arising on a metallic tip at zero potential under the influence of an infinite planar slab of point charges. Again, the solution of such a problem has no straightforward analytical solution. However, we can again use the condition $R \gg R_a$, as depicted, to some extend, in fig.2d. Consequently, the mesoscopic part of the apex can be assumed as equivalent to an infinite planar conductor, at least in a small area along the sides of the asperity (light grey area in fig.2d). The new boundary-value problem defined by an infinite planar conductor influencing another infinite planar conductor at zero potential carrying a hemispherical bump with a radius R_a, now yields a solution[38]. The method of the image charges is used to solve it. The first set of image charges ensuring a zero-potential value on the counter-electrode[39] produces an electric field which influences the tip. But as a matter of fact, this contribution can be neglected because the distance between the tip and the counter-electrode is on the millimeter range and the image charges originate from the Madelung potential, which is known to decay exponentially fast[40,41] (*cf.* also hereafter). The second set of image charges[42] is quasi-punctual and located at the center of the asperity. Hence, owing to the simplified geometry of the electrode, the problem is reduced to a sphere with radius R_a at zero potential in the influence of two infinite planes, *i.e.* the slab and its image, which are anti-symmetrically spaced with respect to the sphere. This procedure ensures a zero-potential on the approximated plane within which the asperity is embedded. Again, it is more convenient to use a spherical coordinate system centered on the asperity. Then, the surface charge density $\sigma_\mu = \sigma_\mu^{(1)} + \sigma_\mu^{(2)}$ is derived by normal derivation along areas (1) and (2), namely:

$$\sigma_\mu = - \underbrace{\epsilon_0 \frac{\partial V_\mu(r,\theta,\varphi)}{\partial r}}_{(1)=\text{asperity}}\Bigg|_{r=R_a} - \underbrace{\epsilon_0 \frac{\partial V_\mu(r,\theta,\varphi)}{r\partial\theta}}_{(2)=\text{planar area}}\Bigg|_{\theta=\pi/2} , \tag{10}$$

The potential V_μ is derived from the Madelung potential of the ionic crystal, previously referred to as V_s, by the method of the image charges and the Kelvin transform (influence

on a sphere biased at zero potential)[38], namely:

$$V_\mu(r,\theta,\varphi) = \left\{V_s(r,\theta,\varphi) - \frac{R_a}{r}V_s\left(\frac{R_a^2}{r},\theta,\varphi\right)\right\}\Big|_{\text{slab}} - \left\{V_s(r,\pi-\theta,\varphi) - \frac{R_a}{r}V_s\left(\frac{R_a^2}{r},\pi-\theta,\varphi\right)\right\}\Big|_{\text{image slab}} \tag{11}$$

The former equation fulfills the boundary condition $V_\mu(r = R_a) = 0$ everywhere along the surface asperity or along the surface of the local planar area around it.

V_s can be estimated on the base of the work by Watson *et al.*[40]. When considering an infinite planar slab of point charges, the authors state that the potential, so-called Madelung surface potential, reaches its asymptotic value in a very short distance normal to the slab. Consequently, the ions within the crystal at a distance only one lattice constant from the surface have Madelung potentials which are indistinguishable from those of the bulk. In other words, *the tip will mainly be influenced by the surface potential and not by the one arising from the bulk part of the ionic crystal.* This is why a single, infinite, layer of point charges is enough to describe the influence of the Madelung surface potential on the tip, which motivates our initial assumption. The potential is written:

$$V_s\left(\overrightarrow{\rho}, z_\mu\right) = \frac{1}{4\pi\epsilon_0}\left(\frac{2\pi}{a'^2}\sum_{\overrightarrow{G}} q(\overrightarrow{G}) e^{i\overrightarrow{G}.\overrightarrow{\rho}} e^{-Gz_\mu}\right), \tag{12}$$

where $\overrightarrow{\rho} = x\widehat{i} + y\widehat{j}$ is the polar vector of any ion of the surface slab in an orthogonal basis $(O, \widehat{i}, \widehat{j})$, O being the projection of the center of the asperity on the surface, $\widehat{i}$ and $\widehat{j}$ the unitary vectors of the fcc unit cell. The summation is performed over the vectors $\overrightarrow{G}$ of the reciprocal lattice of an arbitrarily defined unit cell and a' is proportional to the lattice constant a of the fcc unit cell. $q(\overrightarrow{G})$ is a structure factor:

$$q(\overrightarrow{G}) = \frac{1}{G}\sum_k q_k e^{i\overrightarrow{G}.\overrightarrow{\delta}^{\parallel}_k} e^{G\delta^{\perp}_k} \tag{13}$$

It is summed over the ions within the defined unit cell. The kth ion carries an electrical charge q_k. Its planar and perpendicular coordinates from the origin of the cell are given by the two vectors $\overrightarrow{\delta}^{\parallel}_k$ and $\overrightarrow{\delta}^{\perp}_k$. The latter reflects the polarization effect felt by the ion within the unit cell, previously referred to as $\delta^{\perp}(V_b)$. In equ.13, it is assumed that the polarization of the ions extends all over the (001) surface plane. In any case, it must extend over an much larger area than the tip asperity. This assumption is consistent with the electric field

produced by area (2), which is constant within an area roughly scaling as the mesoscopic tip radius R. V_s is calculated from the unit cell defined in fig.2a (light grey). It consists of 4 anions and a cation weighting for a fourth and one, respectively. The vectors of the direct lattice are $\overrightarrow{\alpha} = a'\widehat{i}$ and $\overrightarrow{\beta} = a'\widehat{j}$, where $a' = a\sqrt{2}/2$. Owing to the exponential decay of the potential with z_μ, visible in equ.12, the calculation of the structure factor can be restricted to the first four reciprocal vectors, namely: $\overrightarrow{G}^{\pm}_{i \text{ or } j} = \pm 2\pi/a'(\widehat{i} \text{ or } \widehat{j})$. The calculation yields:

$$V_s(x, y, z_\mu) = -\frac{q}{\pi\epsilon_0 a'} \cosh[\widetilde{\delta}^{\perp}(V_b)]\widetilde{\chi}(x, y)e^{-\frac{2\pi}{a'}z_\mu} \tag{14}$$

with: $\widetilde{\delta}^{\perp}(V_b) = \frac{2\pi}{a'}\delta^{\perp}(V_b)$ and $\widetilde{\chi}(x, y) = \cos\left[\frac{2\pi}{a'}(x - x_0)\right] + \cos\left[\frac{2\pi}{a'}(y - y_0)\right]$, a spatial modulation term. x_0 and y_0 are the x and y coordinates of the center of the asperity projected onto the unit cell. Setting $x_0 = y_0 = 0$ locates the asperity and therefore the tip on top of an anion, the reference ion within the defined unit cell. The above expression exhibits the expected exponential decaying behavior as a function of z_μ. The potential is reported in fig.3 for $a = 0.66$ nm, $\delta^{\perp} = 11$ pm and $z_\mu = 4$ Å. The value of $\delta^{\perp}$ will be justified in section IV.

The expression of $\sigma_\mu = \sigma_\mu^{(1)} + \sigma_\mu^{(2)}$ can now be derived from equ.10. The calculation of $\sigma_\mu^{(1)}$ yields:

$$\begin{aligned}\sigma_\mu^{(1)} = \tfrac{q}{a'^2} \cosh[\widetilde{\delta}^{\perp}(V_b)] \left\{\widetilde{\chi}(R_a, \theta, \varphi)\mathcal{F}^{(1)}(\theta) - \right. \\ \left. \widetilde{\zeta}(R_a, \theta, \varphi)\mathcal{G}^{(1)}(\theta)\right\} e^{-\frac{2\pi}{a'}(z_\mu + R_a)}\end{aligned} \tag{15}$$

with $\widetilde{\chi}(r, \theta, \varphi)$, the expression of $\widetilde{\chi}(x, y)$ in the spherical coordinate system centered on the asperity and $\widetilde{\zeta}(r, \theta, \varphi)$, the spherical expression of another spatial modulation term given by: $\widetilde{\zeta}(x, y) = (x \sin\left[\frac{2\pi}{a'}(x - x_0)\right] + y \sin\left[\frac{2\pi}{a'}(y - y_0)\right])/\sqrt{x^2 + y^2}$. The functions $\mathcal{F}^{(1)}$ and $\mathcal{G}^{(1)}$ are written:

$$\mathcal{F}^{(1)}(\theta) = \frac{2a'}{\pi R_a} \sinh\left(\frac{\eta_\theta}{2}\right) - 8\cos\theta \cosh\left(\frac{\eta_\theta}{2}\right) \tag{16}$$

and:

$$\mathcal{G}^{(1)}(\theta) = 8\sin\theta \sinh\left(\frac{\eta_\theta}{2}\right) \tag{17}$$

with: $\eta_\theta = 4\pi R_a \cos\theta/a'$ (see also the appendix). Thus, it was necessary to assume area (2) as an infinite plane in order to derive the expression of $\sigma_\mu^{(1)}$ by means of the method of the

images. In such a case, the expression of $\sigma_\mu^{(2)}$ is rigorously derived from equ.10 and is explicitly given in ref.[43]. For x and y positions large compared to R_a however, this description does not fit with the geometry of the tip apex defined in problem B. The "infinite plane" must actually be shrunk down to a spatially limited area around the asperity, as sketched in fig.2d. This is made possible when assuming that any planar area is the asymptotic limit of a sphere with large radius compared to its extension. The former statement is fulfilled by the condition $R \gg R_a$. The surface charge density of a sphere with radius R under the influence of the surface potential V_s is also derivable from the Kelvin transform. Here, the spherical coordinate system is centered on the sphere with radius R. $\sigma_\mu^{(2)}$ is written:

$$\begin{aligned}\sigma_\mu^{(2)} = \tfrac{q}{a'^2}\cosh[\widetilde{\delta}^{\perp}(V_b)]\left\{\mathcal{F}^{(2)}(\theta)\widetilde{\chi}(R,\theta,\varphi) - \right. \\ \left. \mathcal{G}^{(2)}(\theta)\widetilde{\zeta}(R,\theta,\varphi)\right\} e^{-\frac{2\pi}{a'}(z_\mu+R_a)}\end{aligned} \tag{18}$$

The functions $\mathcal{F}^{(2)}$ and $\mathcal{G}^{(2)}$ are written:

$$\mathcal{F}^{(2)}(\theta) = \left(\frac{a'}{\pi R} - 4\cos\theta\right) e^{-\frac{2\pi}{a'}R(\cos\theta+1)} \tag{19}$$

and:

$$\mathcal{G}^{(2)}(\theta) = 4\sin\theta e^{-\frac{2\pi}{a'}R(\cos\theta+1)} \tag{20}$$

Since $\mathcal{F}^{(2)}(\theta)$ and $\mathcal{G}^{(2)}(\theta)$ decrease exponentially fast as one moves away from the foremost position of the tip apex, it can readily be verified that equ.18 and the expression given in ref.[43] do fit for x or $y \in [R_a; 3R_a]$. Thus, even in the vicinity of the asperity, expression 18 can be used instead of ref.[43]. Therefore, the most part of the contribution of the sphere to $\sigma_\mu^{(2)}$ is restricted to a small area that can be assumed as locally planar.

The graph of the projection of σ_μ on the tip apex (areas (1) and (2)) is reported in fig.4 on top of an anion (positive charge density on the asperity) at a distance $z_\mu = 4$ Å from the surface and for $R = 5$ nm and $R_a = 1$ Å. The oscillations of σ_μ at the surface of the tip due to the image charges of the crystal are readily visible, although their amplitude decreases exponentially fast along the sides of the asperity. The relevant oscillations in area (2) spread out in a circular area with only two unit cells radius. Owing to the exponential decay of the Madelung surface potential farther away from the asperity, the tip surface is too far from the crystal surface to produce relevant image charges. On top of the asperity, the surface

charge density reaches about 2×10^{-2} C.m^{-2}. For a half-sphere with radius $R_a = 1$ Å and with $\delta^{\perp} = 11$ pm, this results in a local charge carried by the tip of about 0.8×10^{-2} q.

III. ESTIMATION OF THE FORCE

A. Estimation of F_m

Owing to the geometry of the problem and since σ_m is equivalent to the surface charge density of an isolated, conducting sphere, we can now fully evaluate the purely capacitive component F_m to the total force. The force effectively acting on the mesoscopic part of the tip apex can be derived from the image charge of the sphere $-4\pi R^2 \sigma_m$ placed at a symmetric position with respect to the counter-electrode, *i.e.* at a distance $2h_d$ from the mesoscopic apex:

$$F_m = -\frac{(4\pi R^2 \sigma_m)^2}{4\pi\epsilon_0 (2h_d)^2} = -\frac{\pi R^2}{h_d^2} \widetilde{\epsilon}_d^2 \epsilon_0 V_b^2 \tag{21}$$

With $\epsilon_d \simeq 4.87$ (ref.[44]) and $K = 0.9$ (arbitrarily), then $\widetilde{\epsilon}_d = K\epsilon_d = 4.38$. For a typical ac modulation of the bias of about 0.5 V and considering $R \simeq 5$ nm and $h_d = 5$ mm, the former equation gives an estimation for the mesoscopic component of the electrostatic force: $F_m \simeq 8 \times 10^{-11}$ pN. As suspected, this contribution is negligible compared to the other two components[45]. Therefore the expression of the total force simplifies to:

$$F = F_{m\mu} + F_{\mu} = \int_{\text{tip}} \frac{\sigma_m \sigma_{\mu}}{\epsilon_0} d\mathcal{S} + \int_{\text{tip}} \frac{\sigma_{\mu}^2}{2\epsilon_0} d\mathcal{S} \tag{22}$$

The reason why the tip has been restricted to its apex is now clear. Regarding the former capacitive force, owing to the distance between the tip and the counter-electrode, the contribution of a macroscopic body in addition to the mesoscopic apex would not change notably the total force. Regarding the other force components, $F_{m\mu}$ and F_{μ}, owing to the exponential decay of the Madelung surface potential, the influence of the macroscopic body of the tip is expected to be negligible as well.

B. Estimation of F_μ

Let us first focus on F_μ. The integral must be performed over the asperity and the mesoscopic sphere around it, areas (1) and (2), respectively. It is recalled that the two areas do not overlap each together. For each of them, the spherical coordinate system must be centered on the corresponding sphere. Thus:

$$\begin{aligned} F_\mu = F_\mu^{(1)} + F_\mu^{(2)} = \frac{R_a^2}{2\epsilon_0} \int_{\frac{\pi}{2}}^{\pi} \int_0^{2\pi} \cos\theta \sin\theta {\sigma_\mu^{(1)}}^2 d\theta d\varphi + \\ \frac{R^2}{2\epsilon_0} \int_{\frac{\pi}{2}}^{\theta_M} \int_0^{2\pi} \cos\theta \sin\theta {\sigma_\mu^{(2)}}^2 d\theta d\varphi \end{aligned} \tag{23}$$

The radial coordinates are fixed to $r = R_a$ and $r = R$ in areas (1) and (2), respectively. The polar integration in area (1) is performed with $\theta \in [\pi/2; \pi]$, whereas in area (2), it is performed with $\theta \in [\pi/2; \theta_M]$, where $\theta_M = \pi - \arcsin(R_a/R)$, which ensures the continuity from (1) to (2). Regarding area (2), the choice of the beginning angle of the interval ($\pi/2$) does not influence notably the result of the integration. In other words, owing to the exponential decay of $\sigma_\mu^{(2)}$, the exact shape of the mesoscopic part of the tip apex far from the asperity is not relevant. This justifies *a posteriori* the choice, although simple, of a spherical geometry. Both integrations over the azimuthal angle must be performed over $\varphi \in [0; 2\pi]$. Note that in each of the former integrals, the term $\cos\theta$ stands for the vertical projection of the force, as stated initially. Although the integration over the azimuthal angle yield an analytical result, the integration over θ does not, which requires to evaluate some integrals numerically. The expression of $F_\mu^{(1)}$ is written:

$$\begin{aligned} F_\mu^{(1)} = \frac{q^2 R_a^2}{2\epsilon_0 a'^4} \cosh^2[\widetilde{\delta}^\perp(V_b)] e^{-\frac{4\pi}{a'}(z_\mu + R_a)} \left\{ A^{(1)} + \right. \\ \left. B^{(1)} \left[\cos(\widetilde{x}_0) + \cos(\widetilde{y}_0)\right] + 2C^{(1)} \cos(\widetilde{x}_0) \cos(\widetilde{y}_0) \right\} \end{aligned} \tag{24}$$

with: $\widetilde{x}_0 = 2\pi x_0/a'$ and $\widetilde{y}_0 = 2\pi y_0/a'$, the reduced coordinates of the tip above the crystal surface. The integral forms of coefficients $A^{(1)}$, $B^{(1)}$ and $C^{(1)}$ are reported in the appendix as functions of R_a and a'. Taking a typical lattice constant for alkali halides $a' = a\sqrt{2}/2 \simeq 0.45$ nm and assuming $R_a \simeq 1$ Å, we get:

$$A^{(1)} \simeq -130 \quad B^{(1)} \simeq -70 \quad C^{(1)} \simeq A^{(1)} \simeq -130 \tag{25}$$

Thus, $F_\mu^{(1)}$ explicitly depends on the spatial modulation of the surface potential. Note also the exponential decay with the distance, actually faster than the distance dependence of the

Madelung surface potential and also the doubling spatial period term.

Similar integration on area (2) yields:

$$F_{\mu}^{(2)} = \frac{q^2R^2}{2\epsilon_0 a'^4}\cosh^2[\widetilde{\delta}^{\perp}(V_b)]e^{-\frac{4\pi}{a'}(z_\mu+R_a)}\left\{A^{(2)}+ B^{(2)}\left[\cos\left(\widetilde{x}_0\right)+\cos\left(\widetilde{y}_0\right)\right]+2C^{(2)}\cos\left(\widetilde{x}_0\right)\cos\left(\widetilde{y}_0\right)\right\} \tag{26}$$

The integral forms of coefficients $A^{(2)}$, $B^{(2)}$ and $C^{(2)}$ are derived from those of coefficients $A^{(1)}$, $B^{(1)}$ and $C^{(1)}$, by replacing R_a, $\mathcal{F}^{(1)}(\theta)$ and $\mathcal{G}^{(1)}(\theta)$ with R, $\mathcal{F}^{(2)}(\theta)$ and $\mathcal{G}^{(2)}(\theta)$, respectively. The integration is now performed with $\theta \in [\pi/2; \theta_M]$. With similar parameters than before and setting $R = 5$ nm, we now get:

$$A^{(2)} \simeq -8 \quad B^{(2)} \simeq C^{(2)} \simeq 0 \tag{27}$$

The striking discrepancy between $A^{(2)}$, $B^{(2)}$ and $C^{(2)}$ is due to the combined contribution of the Bessel functions and the exponential decay of the functions $\mathcal{F}^{(2)}(\theta)$ and $\mathcal{G}^{(2)}(\theta)$ occurring in the integral forms of the coefficients $B^{(2)}$ and $C^{(2)}$. Hence, the force simplifies to:

$$F_{\mu}^{(2)} = \frac{q^2R^2}{2\epsilon_0 a'^4}\cosh^2[\widetilde{\delta}^{\perp}(V_b)]e^{-\frac{4\pi}{a'}(z_\mu+R_a)}A^{(2)} \tag{28}$$

The spatial modulation of the potential does not influence the mesoscopic part of tip while scanning the surface. This contribution acts as a static shift to the total electrostatic force, similarly as the Van der Waals long-range interaction for the short-range chemical interactions which are responsible for the topographic atomic contrast in nc-AFM.

C. Estimation of $F_{m\mu}$

The geometrical splitting in terms of areas (1) and (2) used for the estimation of F_μ, can equivalently be applied to $F_{m\mu}$. Thus:

$$\begin{aligned} F_{m\mu} &= F_{m\mu}^{(1)} + F_{m\mu}^{(2)} = \\ &\frac{R_a^2}{\epsilon_0}\int_{\frac{\pi}{2}}^{\pi}\int_0^{2\pi}\cos\theta\sin\theta\sigma_m^{(1)}\sigma_\mu^{(1)}d\theta d\varphi + \\ &\frac{R^2}{\epsilon_0}\int_{\frac{\pi}{2}}^{\theta_M}\int_0^{2\pi}\cos\theta\sin\theta\sigma_m^{(2)}\sigma_\mu^{(2)}d\theta d\varphi \end{aligned} \tag{29}$$

$\sigma_m^{(1)}$ and $\sigma_m^{(2)}$ are the surface charge densities on areas (1) and (2) within the frame of problem

A. The calculation of $F_{m\mu}^{(1)}$ yields:

$$F_{m\mu}^{(1)} = \frac{3\widetilde{\epsilon}_d q R_a^2}{a'^2 R} V_b \cosh[\widetilde{\delta}^{\perp}(V_b)] e^{-\frac{2\pi}{a'}(z_\mu + R_a)} \times D^{(1)} \left[\cos\left(\widetilde{x}_0\right) + \cos\left(\widetilde{y}_0\right)\right] \tag{30}$$

The integral form of $D^{(1)}$ is reported in the appendix. The numerical integration results in $D^{(1)} \simeq -15$. Similar integration over area (2) gives a similar expression of $F_{m\mu}^{(2)}$ by replacing indexes (1) with indexes (2) and R_a with R. The integral form of the coefficient $D^{(2)}$ is similar to the one of $D^{(1)}$, except that the term $\cos^2\theta$ is replaced by $\cos\theta$. The numerical integration of $D^{(2)}$ yields almost zero. This was expected since the integration is performed over the oscillations of the charge density $\sigma_\mu^{(2)}$ due to the image charges of the surface potential (*cf.* fig.4). On the opposite, this was not observed in $F_\mu^{(2)}$ because the integration was performed on the square of $\sigma_\mu^{(2)}$. Therefore $F_{m\mu}$ is finally written:

$$F_{m\mu} = F_{m\mu}^{(1)} \tag{31}$$

Hence, the former equation states that the coupling of the force to the bias V_b actually occurs only by means of the microscopic surface charge density at the foremost part of the tip, *i.e.* on the asperity. Owing to the integration over the mesoscopic part of the tip apex and the subsequent cancellation due to the oscillations of $\sigma_\mu^{(2)}$, no relevant coupling between the bias voltage and the mesoscopic part of the tip apex can occur. This aspect strongly suggests that the effect we are reporting is mainly controlled by the foremost structure of the tip. The effect is expected to be much enhanced in case of tips with sharper geometries, particularly those with apexes including atomically sharp edges.

The expression for the vertical contribution of the total force acting on the tip due to the combined influence of the capacitive coupling and of the Madelung surface potential is finally written: $F = F_{m\mu} + F_\mu = F_{m\mu}^{(1)} + F_\mu^{(1)} + F_\mu^{(2)}$, with $F_{m\mu}^{(1)}$ given by equ.30, $F_\mu^{(1)}$ by equ.24 and $F_\mu^{(2)}$ by equ.28. The graph of the total force and of its components is reported in fig.5 for similar parameters than previously, namely: $a = 0.66$ nm, $\delta^{\perp} = 11$ pm and $z_\mu = 4$ Å. A typical value of bias has been set, $V_b = +1$ V. Thus, it is visible that the term $F_\mu^{(1)}$ is negligible compared to others. This is due to the prefactor R_a^2/a'^4 *vs.* R^2/a'^4 for $F_\mu^{(2)}$. The total electrostatic force F finally simplifies to:

$$F = F_{m\mu}^{(1)} + F_\mu^{(2)} \tag{32}$$

In fig.5, the force reaches an average value of about 9 pN (absolute value) and a corrugation of about 2 pN (peak to peak).

IV. IMPLICATIONS FOR KPFM

A. Estimation of $\delta^{\perp}(V_b)$

The net displacement $\delta^{\perp}(V_b)$ of the topmost ionic layer induced by the polarization can be estimated out of the electric field $\overrightarrow{E}$ between the tip and the surface (*cf.* equ.2). Section II A has shown that the field induced by the bias voltage was essentially controlled by the mesoscopic radius of the tip, R, and not by the foremost asperity. Therefore, owing to equs.4 or 8: $E \simeq V_b/R$. The expression of $\delta^{\perp}(V_b)$ can now be deduced using equ.2:

$$\delta^{\perp}(V_b) = \frac{\chi_d}{q} E = V_b \frac{\chi_d}{qR} \tag{33}$$

An order of magnitude for $\delta^{\perp}(V_b)$ can now be calculated as follows: with $V_b \simeq 1$ V, $R = 5$ nm, $\alpha_i = 70 \times 10^{-30}$ m^3 (ref.[36]) and $n_v = 8\sqrt{2}/a^3 \simeq 40 \times 10^{27}$ m^{-3} (number of polarizable ionic species *per* volume unit in a fcc crystal of KBr with a lattice constant $a = 0.66$ nm), we get $E = 2 \times 10^8$ V.m^{-1}, $\chi_d \simeq 9 \times 10^{-39}$ F.m^2 and therefore $\delta^{\perp} \simeq 11$ pm.

B. Detected signal in KPFM: connection with the local CPD

When performing KPFM experiments, the bias voltage V_b is modulated with a frequency f_k and may as well include a static component to compensate for the long-range electrostatic forces. This is the reason why the average value of the experimental CPD image shown in fig.1a reaches -3.9 V. It is not rare that, on ionic surfaces, many volts are required to compensate for the long-range electrostatic forces due to trapped charges while the cleavage of the cristal[16]. Thus:

$$V_b = V_{dc} + V_{ac} \sin(2\pi f_k t) \tag{34}$$

The electrostatic force is thus triggered at f_k and then detected as an additional low- or high-frequency component when doing FM- or AM-KPFM, respectively. In both techniques, a proper dc bias voltage produced by an external controller, hereafter referred to as $V_{dc}^{(c)}$, is

applied between the tip and the counter-electrode to cancel the modulated component at f_k, *i.e.* the oscillation amplitude of the second bending eigenmode of the cantilever in AM-KPFM, or the one of the frequency shift in FM-KPFM. When applied to the tip (*i.e.* with the counter-electrode grounded), this dc bias is the opposite of the local CPD defined in equ.1: $V_{dc}^{(c)} = -V_{\mathrm{cpd}}$.

In order to stick to the AM-KPFM experiments (fig.1), it is necessary to estimate the amplitude of the second eigenmode of the cantilever and then derive a condition on the dc value of the bias ultimately able to nullify it. On the one hand, it is therefore mandatory to check carefully all the occurrences of the modulated component of the bias voltage in the expression of the force. This includes explicit dependencies, such as those due to the polarization, but also implicit ones, as discussed hereafter. On the other hand, an expression of the oscillation amplitude of the mode modulated at f_k must be derived.

We first address the problem of explicit and implicit bias dependencies in the expression of the electrostatic force. Owing to the explicit V_b dependence in $\delta^{\perp}$, which has been kept throughout the description of the model, it can be seen that the polarization effect is mainly included in the cosh function of $F_{m\mu}^{(1)}$ and $F_{\mu}^{(2)}$ through a linear and a quadratic dependence, respectively (*cf.* equs.30 and 28). Furthermore, since $\delta^{\perp}$ is small compared to a', $\cosh[\widetilde{\delta}^{\perp}(V_b)]$ can be expanded in series. To first order:

$$\cosh[\widetilde{\delta}^{\perp}(V_b)] \simeq 1 + \widetilde{\delta}^{\perp}(V_b)^2 = 1 + \frac{4\pi^2}{a'^2}\delta^{\perp}(V_b)^2 = 1 + (\chi'_d V_b)^2 \tag{35}$$

with $\chi'_d = 2\pi\chi_d/(a'qR)$. Replacing this expansion in the expressions of the components of the force and keeping the linear and quadratic terms in V_b yields, with compact notations:

$$F_{m\mu}^{(1)} = \widetilde{\epsilon}_d K_{m\mu}^{(1)} \Phi_{m\mu}^{(1)} \frac{qV_b}{R} \tag{36}$$

and:

$$F_{\mu}^{(2)} = K_{\mu}^{(2)} \Phi_{\mu}^{(2)} [1 + 2(\chi'_d V_b)^2] \frac{q^2}{\epsilon_0 a'^2}, \tag{37}$$

where $K_{m\mu}^{(1)}$ and $K_{\mu}^{(2)}$ are two dimensionless coefficients standing for geometrical factors of areas (1) and (2), respectively:

$$K_{m\mu}^{(1)} = \frac{3R_a^2}{a'^2} D^{(1)} \quad \text{and} \quad K_{\mu}^{(2)} = \frac{R^2}{2a'^2} A^{(2)} \tag{38}$$

$\Phi^{(1)}_{m\mu}$, $\Phi^{(2)}_{\mu}$ are also two dimensionless coefficients carrying the spatial dependence of each force component:

$$\Phi^{(1)}_{m\mu} = e^{-\frac{2\pi}{a'}(z_\mu + R_a)} \left[\cos\left(\widetilde{x}_0\right) + \cos\left(\widetilde{y}_0\right)\right] \tag{39}$$

and:

$$\Phi^{(2)}_{\mu} = e^{-\frac{4\pi}{a'}(z_\mu + R_a)} \tag{40}$$

Implicit V_b dependencies are now discussed. In the two former equations, particular attention must be paid to z_μ. So far, this parameter was defined as the tip-surface distance and set to an arbitrary, constant, value. However, when dealing with AM-KPFM, z_μ is not static but actually coupled to the bias and to the oscillation amplitude of the fundamental eigenmode of the cantilever. In the following, for the sake of clarity, the variables related to the fundamental eigenmode of the cantilever will be denoted with index "0" and those of the second eigenmode with index "1". Thus, let z_0, z_1 and D be the instantaneous position of the fundamental eigenmode of the cantilever, the instantaneous position of the second eigenmode of the cantilever and the distance between the surface and the equilibrium position of the cantilever at rest, respectively. Therefore, $z_\mu(t) = D - z_0(t) - z_1(t)$. Hence, if V_b has the form given in equ.34, one can postulate, to first order: $z_1(t) = A_1 \sin(2\pi f_k t + \varphi_1)$. A_1 and φ_1 stand for the oscillation amplitude of this mode and its phase lag with respect to the electrostatic actuation, respectively. Their exact expressions are not easily derivable, but it must be noticed that A_1 must be connected to the amplitude of the modulation, namely V_{ac}. When f_k accurately matches the actual resonance frequency of the second eigenmode[46], then $\varphi_1 = -\pi/2$. z_0 is experimentally driven by the control electronics of the microscope at the actual resonance frequency of the fundamental mode of the cantilever, f_0. It is known that it has an almost harmonic behavior of the form: $z_0(t) = A_0 \sin(2\pi f_0 t - \pi/2)$. Thus, $\Phi^{(1)}_{m\mu}$ and $\Phi^{(2)}_{\mu}$ have a component at f_0 which is further modulated by the dynamics of the second eigenmode, electrostatically actuated at f_k.

We can now propose a self-consistent approximated solution to the equation of motion for $z_1(t)$ and thus derive the expression of the oscillation amplitude A_1. This equation has

the standard form:

$$\ddot{z_1}(t) + \frac{\omega_1}{Q_1}\dot{z_1}(t) + \omega_1^2 z_1(t) = \frac{F_{ext}}{m_1} + \frac{F_{m\mu}^{(1)} + F_{\mu}^{(2)}}{m_1}, \tag{41}$$

where F_{ext} is an external force oscillating at f_0 which controls the dynamics of $z_0(t)$. Let us assume: i- $A_1 \ll A_0$, *i.e.* the amplitude of the mode is much smaller than the one of the fundamental mode, ii- $A_1 \ll a'$, where $a' = a\sqrt{2}/2$, a being the lattice constant of the crystal and iii- that the dynamics of $z_1(t)$ is mainly influenced by components at f_k. Assumptions i- and ii- are not too strong, since the experimental estimations of A_1 yield a few tens of picometers. Assumption i- implies that the dynamics of the fundamental mode is not much influenced by the one of the second eigenmode. Hence, the solution of the equation of motion of $z_0(t)$ has indeed the form postulated above. Assumption ii- allows us to linearize $\Phi_{m\mu}^{(1)}$ and $\Phi_{\mu}^{(2)}$ with respect to $z_1(t)$. Finally, assumption iii-, which is consistent with the postulated solution for $z_1(t)$, $z_1(t) = A_1 \sin(2\pi f_k t + \varphi_1)$, simplifies further the above equation of motion. Now, owing to the former assumptions, equ.41 can be solved by injecting the postulated expressions of both eigenmodes and keeping only the terms oscillating at f_k. For that purpose, the exponential term wherein $z_0(t)$ occurs must be expanded in Fourier series. Then, the only possibility to preserve terms at f_k is to keep the lone static component of the Fourier expansion, hereafter referred to as a_0 (expansion of $\Phi_{m\mu}^{(1)}$) and b_0 (exansion of $\Phi_{\mu}^{(2)}$). After linearization, $\Phi_{m\mu}^{(1)}$ and $\Phi_{\mu}^{(2)}$ can finally be written as:

$$\begin{aligned} \Phi_{m\mu}^{(1)} &\overbrace{\simeq}^{\text{i-, ii-}} \left[1 - \tfrac{2\pi}{a'} z_1(t)\right] e^{-\frac{2\pi}{a'}(D - A_0 + R_a)} \times \\ \{a_0 + \underbrace{\sum_{n=1}^{\infty} a_n \cos(2\pi n f_0 t)}_{\text{neglected, owing to iii-}}\} &\left[\cos\left(\widetilde{x}_0\right) + \cos\left(\widetilde{y}_0\right)\right] \end{aligned} \tag{42}$$

and:

$$\Phi_{\mu}^{(2)} \simeq \left[1 - \frac{4\pi}{a'} z_1(t)\right] e^{-\frac{4\pi}{a'}(D - A_0 + R_a)} \{b_0 + \underbrace{\sum_{n=1}^{\infty} b_n \cos(2\pi n f_0 t)}_{\text{neglected, owing to iii-}}\} \tag{43}$$

With:

$$\begin{aligned} a_n &= e^{-\frac{2\pi}{a'} A_0} I\left[n, \tfrac{2\pi}{a'} A_0\right] \\ b_n &= e^{-\frac{4\pi}{a'} A_0} I\left[n, \tfrac{4\pi}{a'} A_0\right] \end{aligned} \tag{44}$$

I is the modified Bessel function of the first kind. When replacing equs.42 and 43 with $z_1(t) = A_1 \sin(2\pi f_k t + \varphi_1)$ in equ.41, it is possible to derive an expression for A_1. The condition on $V_{dc}^{(c)}$ to match $A_1 = 0$ is finally written:

$$V_{dc}^{(c)} = -\frac{\widetilde{\epsilon}_d \epsilon_0 a'^2}{4Rq{\chi'_d}^2} \frac{a_0}{b_0} \frac{K_{m\mu}^{(1)}}{K_\mu^{(2)}} e^{\frac{2\pi}{a'}(D+R_a-A_0)} [\cos(\widetilde{x_0}) + \cos(\widetilde{y_0})] \tag{45}$$

The graph of $V_{dc}^{(c)}$ is reported in fig.6 for $a = 0.66$ nm, $\delta^\perp = 11$ pm, $A_0 = 5$ nm (hence $a_0 = 0.0487$ and $b_0 = 0.0344$) and $(D - A_0) = 3.5$ Å. The value of A_0 has been chosen consistently with the experimental conditions. On the contrary, the tip-surface distance has been chosen arbitrary, but however in a range where the atomic contrast is usually experimentally achieved. In fig.6, the lateral periodicity of the underlying lattice is readily visible, but surprisingly, the potential scales between -0.6 to +0.6 V from an anionic to a cationic site, respectively. At similar height, this is three times larger than the Madelung surface potential (*cf.* fig.3b). The comparison with the experimental results is more severe since the theoretical prediction is one order of magnitude larger. At this point, it is recalled that the strong tip geometry dependence of the problem makes a straightforward comparison between the theoretical prediction (equ.45) and the experimental results difficult, since our analytical expression of $V_{dc}^{(c)} = -V_{cpd}$ relies on a somewhat unrealistic tip.

C. Experimental implications for AM-KPFM

The figure and the above formula show that the bias voltage to be applied on the tip to compensate for the electrostatic force is governed by three main factors:

- the dielectric properties of the sample such as its dielectric permittivity and lattice constant.
- a subtle balance between mesoscopic and microscopic geometric factors of the tip.
- a lateral periodicity similar to the Madelung surface potential of the crystal.

A straightforward consequence is that the atomic corrugation of the CPD reported experimentally might stand for the spatial fluctuations of the Madelung surface potential, however with an amplitude that depends on the surface polarization and hence on the applied ac voltage. It is also important to notice that the CPD compensation is proportional

to $K^{(1)}_{m\mu}$, *i.e.* to the asperity size. The former being also the source of the coupling between the tip/dieletric/counter-electrode capacitor and the Madelung surface potential, *i.e.* the source of the KPFM signal, the atomic contrast of the CPD is therefore closely connected with the geometry of the very foremost part of the tip. This is consistent with the short-range character of the interaction. But, on the other hand, the explicit dependence with geometric factors of the tip, unambiguously proves that quantitative measurements of the local CPD are unlikely to be performed in KPFM, unless the tip geometry be accurately known, which is practically never true.

Furthermore, although equ.45 explicitly exhibit a distance dependence, consistently with the experimental observations in the above mentioned references, an increase of the compensated CPD as a function of the distance is nevertheless surprising. The residual exponential dependence originates from $\Phi^{(2)}_{\mu}$, *i.e.* from the influence of the Madelung surface potential on the mesoscopic tip apex. As discussed above, the CPD compensation being partly governed by the asperity, a tip-surface distance increase Δz_{μ} produces a decrease of the related force $F^{(1)}_{m\mu}$ proportional to $\exp\left(-2\pi\Delta z_{\mu}/a'\right)$ (*cf.* $\Phi^{(1)}_{m\mu}$, equs.39 or 42). This abrupt change is compensated by an equivalent exponential increase of the compensated CPD. This process can obviously not occur at any tip-surface distance. Prior to being cancelled, the f_k component must stand for a measurable signal. Therefore the above discussion stands within a narrow range of distances from the surface, typically a few times the asperity radius.

Nevertheless, an increase of the measured local CPD as a function of the distance is still expected to occur if the distance dependence in $\Phi^{(2)}_{\mu}$ decays faster than the one in $\Phi^{(1)}_{m\mu}$. In other words $V^{(c)}_{dc}$ must increase with the distance as soon as the distance dependence of the force induced by the influence of the Madelung surface potential on the mesoscopic part of the tip decays faster than the one of the force induced on the asperity due to the capacitive coupling with the image charges of the surface.

Let us finally point out that such a distance dependence of the CPD might make the experimental achievement of the atomic contrast easier, which strengthens the argument of an intrinsic imaging process of the local CPD. Indeed, no major tip and/or surface distortion is expected to occur in an equivalent range of distance ($\geq$ 3 Å, ref.[47]). In that case, instabilities due to adsorbed and/or mobile atomic or ionic species at the tip apex are less likely to occur, which makes the imaging process robust, as experimentally observed.

To conclude, the analytical approach, although restricted to a tip with a basic geometry, remains helpful, primarily because it provides an expression of the short-range electrostatic force that can be connected to the nc-AFM-KPFM simulator. There are obvious limitations to our approach, the most important one being the use of classical, continuous electrostatics to treat the angstrom-size nanoasperity. This obviously must break down at a certain point, and be replaced by a proper quantum mechanical treatment of the problem. In the near future, the electrostatic model should be extended to a bit more complex systems such as local dipoles, charges or defects at the surface and at steps of ionic crystals.

V. CONCLUSION

The aim of this work was to provide a consistent approach to describe the short-range electrostatic force between the tip of an nc-AFM and the (001) surface of a perfect ionic crystal. In order to develop an analytical expression for the total electrostatic force, the tip has been restricted to a simple geometry and the influence of the sample has been described by means of its Madelung surface potential. In such a way, an analytical solution for the total electrostatic force was found within the boundary-value problem assuming a thick dielectric sample and an infinite top-layer of ionic surface charges.

Two major contributions to the electrostatic force can be extracted: the first stands for a coupling term between the microscopic structure of the tip apex and the capacitor formed between the tip, the dielectric ionic crystal and the counter-electrode due to the bias voltage V_b; the second term depicts the influence of the fluctuations of the Madelung surface potential arising at the surface of the ionic crystal on the mesoscopic part of the tip, independently from its microscopic structure. The former has the lateral periodicity of the Madelung surface potential whereas the latter only acts as a static component which shifts the total force.

Beyond the dielectric properties of the crystal, which are explicitly included in the model, the ionic polarization of the sample due to the influence of the bias voltage applied to the tip/counter-electrode capacitor is mainly responsible for the atomic contrast of the KPFM signal. Typical orders of magnitude give a net displacement of the ions of about ± 10 pm from their equilibrium positions. Note that this displacement only occurs if a tip-sample bias is applied (ac or dc), which is always the case in KPFM experiments.

A detailed analysis of the bias voltage required to compensate for the electrostatic force shows that the compensated CPD has the lateral periodicity of the Madelung surface potential. However, there is a strong dependence on the tip geometry, the applied modulation voltage as well as the tip-sample distance, which can even lead to an overestimation of the real surface potential.

For a quantitative evaluation of KPFM results, it is thus essential to account for all the parameters of the experiment, among which the tip shape. The analytical expression developed in this work provides an alternative tool to elucidate the contrast formation in KPFM on ionic crystals, and in combination with the nc-AFM simulator it might enable us to interpret our results more accurately.

APPENDIX

After integration of $F_\mu^{(1)}$ over the azimuthal angle $\varphi \in [0; 2\pi]$, we have:

$$\begin{aligned} F_\mu^{(1)} = \tfrac{q^2 R_a^2}{2\epsilon_0 a'^4} \cosh^2[\widetilde{\delta}^{\perp}(V_b)] e^{-\frac{4\pi}{a'}(z_\mu + R_a)} \left\{ A^{(1)} + \right. \\ \left. B^{(1)} \left[\cos\left(\widetilde{x}_0\right) + \cos\left(\widetilde{y}_0\right)\right] + 2C^{(1)} \cos\left(\widetilde{x}_0\right) \cos\left(\widetilde{y}_0\right) \right\} \end{aligned} \tag{46}$$

where:

$$A^{(1)} = \pi \int_{\frac{\pi}{2}}^{\pi} \cos\theta \sin\theta [2{\mathcal{F}^{(1)}}^2(\theta) + {\mathcal{G}^{(1)}}^2(\theta)] d\theta \tag{47}$$

$$\begin{aligned} B^{(1)} = \pi \textstyle\int_{\frac{\pi}{2}}^{\pi} \cos\theta \sin\theta \left\{ \left({\mathcal{F}^{(1)}}^2(\theta) - \frac{{\mathcal{G}^{(1)}}^2(\theta)}{2} \right) J_0\left(\eta_\theta\right) - \right. \\ \left. 2\mathcal{F}^{(1)}(\theta)\mathcal{G}^{(1)}(\theta) J_1\left(\eta_\theta\right) + \frac{{\mathcal{G}^{(1)}}^2(\theta)}{2} J_2\left(\eta_\theta\right) \right\} d\theta \end{aligned} \tag{48}$$

and:

$$\begin{aligned} C^{(1)} = \pi \textstyle\int_{\frac{\pi}{2}}^{\pi} \cos\theta \sin\theta \left\{ 2{\mathcal{F}^{(1)}}^2(\theta) J_0\left(\eta'_\theta\right) - \right. \\ 2\sqrt{2}\mathcal{F}^{(1)}(\theta)\mathcal{G}^{(1)}(\theta) J_1\left(\eta'_\theta\right) + \\ \left. {\mathcal{G}^{(1)}}^2(\theta) J_2\left(\eta'_\theta\right) \right\} d\theta \end{aligned} \tag{49}$$

with: $\eta_\theta = 4\pi R_a \sin\theta / a'$ and $\eta'_\theta = 2\sqrt{2}\pi R_a \sin\theta / a'$. J_0, J_1 and J_2 are the Bessel functions of the first kind.

Regarding $F^{(1)}_{m\mu}$, the integration over the azimuthal angle $\varphi \in [0; 2\pi]$ yields:

$$F^{(1)}_{m\mu} = \frac{3\widetilde{\epsilon}_d q R_a^2}{a'^2 R} \cosh[\delta_\perp(V_b)] V_b D^{(1)} \left[\cos\left(\frac{2\pi}{a'} x_0\right) + \cos\left(\frac{2\pi}{a'} y_0\right)\right] \tag{50}$$

where:

$$D^{(1)} = -2\pi \int_{\frac{\pi}{2}}^{\pi} \cos^2\theta \sin\theta \left\{\mathcal{F}^{(1)}(\theta) J_0\left(\frac{\eta_\theta}{2}\right) - \mathcal{G}^{(1)}(\theta) J_1\left(\frac{\eta_\theta}{2}\right)\right\} d\theta \tag{51}$$

References

[1] S. Sadewasser and M. Lux-Steiner, Phys. Rev. Lett. **91**, 266101 (2003).

[2] J. Weaver and D. Abraham, J. Vac. Sci. Technol. B **9**, 1559 (1991).

[3] M. Nonnenmacher, M. O'Boyle, and H. Wickramasinghe, Appl. Phys. Lett. **58**, 2921 (1991).

[4] S. Kitamura and M. Iwatsuki, Appl. Phys. Lett. **72**, 3154 (1998).

[5] A. Kikukawa, S. Hosaka, and R. Imura, Rev. Sci. Instrum. **67**, 1463 (1996).

[6] C. Sommerhalter, T. Matthes, T. Glatzel, A. Jäger-Waldau, and M. Lux-Steiner, Appl. Phys. Lett. **75**, 286 (1999).

[7] T. Glatzel, S. Sadewasser, and M. Lux-Steiner, Appl. Surf. Sci. **210**, 84 (2003).

[8] A. Kikukawa, S. Hosaka, and R. Imura, Appl. Phys. Lett. **66**, 3510 (1995).

[9] V. Palermo, M. Palma, and P. Samorì, Adv. Mater. **18**, 145 (2006).

[10] A. Sasahara, H. Uetsuka, and H. Onishi, Phys. Rev. B **64**, 121406 (2001).

[11] Y. Sugawara, T. Uchihashi, M. Abe, and S. Morita, Appl. Surf. Sci. **140**, 371 (1999).

[12] S. Kitamura, K. Suzuki, M. Iwatsuki, and C. Mooney, Appl. Surf. Sci. **157**, 222 (2000).

[13] K. Okamoto, K. Yoshimoto, Y. Sugawara, and S. Morita, Appl. surf. Sci. **210**, 128 (2003).

[14] F. Krok, J. Kolodziej, B. Such, P. Czuba, P. Struski, P. Piatkowski, and M. Szymonski, Surf. Sci. **566-568**, 63 (2004).

[15] C. Loppacher, U. Zerweck, and L. Eng, Nanotechnology **15**, S9 (2004).

[16] C. Barth and C. Henry, Nanotechnology **17**, S155 (2006).

[17] C. Barth and C. Henry, Phys. Rev. Lett. **98**, 136804 (2007).

[18] L. Howald, E. Meyer, R. Lühi, H. Haefke, R. Overney, H. Rudin and H.-J. Güntherodt, Appl. Phys. Lett. **68**, 117 (1993).

[19] K. Wandelt, Appl. Surf. Sci. **111**, 1 (1997).

[20] R. Hoffmann, L. Kantorovich, A. Baratoff, H. Hug, and H.-J. Güntherodt, Phys. Rev. Lett. **92**, 146103 (2004).

[21] R. Hoffmann, A. Baratoff, H. Hug, H.-R. Hidber, H.v Löhneysen, and H.-J. Güntherodt, Nanotechnology **18**, 395503 (2007).

[22] L. Kantorovich, T. Trevethan, and A. Foster, SciFi, Program for calculation of the Self Consistent Image Force Interaction (2003), v3.51. `http://www.cmmp.ucl.ac.uk /~lev/codes/SciFi/manual_3_51 /index.html`.

[23] S. Lyuksyutov, P. Paramonov, R. Sharipov, and G. Sigalov, Phys. Rev. B **70**, 174110 (2004).

[24] H. Jacobs, P. Leuchtmann, O. Homan, and A. Stemmer, J. Appl. Phys. **84**, 1168 (1998).

[25] J. Colchero, A. Gil, and A. Beró, Phys. Rev. B **64**, 245403 (2001).

[26] H. McMurray and G. Williams, J. Appl. Phys. **91**, 1673 (2002).

[27] S. Sadewasser, T. Glatzel, R. Shickler, Y. Rosenwaks, and M. Lux-Steiner, Appl. Surf. Sci. **210**, 32 (2003).

[28] Y. Rosenwaks, R. Shikler, T. Glatzel, and S. Sadewasser, Phys. Rev. B **70**, 085320 (2004).

[29] T. Takahashi and S. Ono, Ultramicroscopy **100**, 287 (2004).

[30] E. Palacios-Lidón, J. Abellán, J. Colchero, C. Munuera, and C. Ocal, Appl. Phys. Lett. **87**, 154106 (2005).

[31] U. Zerweck *et al.*, Phys. Rev. B **71**, 125424 (2005).

[32] C. Leendertz, F. Streicher, M. Lux-Steiner, and S. Sadewasser, Appl. Phys. Lett. **89**, 113120 (2006).

[33] U. Zerweck, C. Loppacher, T. Otto, S. Grafström, and L. Eng, Nanotechnology **18**, 084006 (2007).

[34] L. Nony *et al.*, Phys. Rev. B **74**, 235439 (2006).

[35] The ionic polarizability α_i is connected to the dielectric permittivity ϵ_d by Claussius-Mossotti's equation.

[36] C. Kittel, *Introduction to Solid State Physics*, 8^{th} ed. (Wiley, New York, 2004).

[37] J. Jackson, *Classical Electrodynamics*, 3^{rd} ed. (Wiley, New York, 1998).

[38] E. Durand, *Electrostatique et Magnétostatique* (Masson, Paris, 1953).

[39] The latter is obtained by anti-symmetrical transform of the charges layer with respect to the counter-electrode symmetry plane.

[40] R. Watson, J. Davenport, M. Perlam, and T. Sham., Phys. Rev. B **24**, 1791 (1981).

[41] This is also true because it has been assumed that the ionic crystal carried no net charge. Therefore there is no long-range electrostatic interaction.

[42] The latter is now obtained by anti-symmetrical transform of the layer of ionic charges into the asperity.

[43] The expression of $\sigma_\mu^{(2)}(r > R_a, \theta = \pi/2, \varphi)$ for an infinite planar geometry is: $\sigma_\mu^{(2)} = \frac{q}{a'^2}\cosh[\delta^\perp(V_b)]\{4\widetilde{\chi}(R,\pi/2,\varphi) - 4\frac{R^3}{r^3}\widetilde{\chi}(R^2/r,\pi/2,\varphi)\}$.

[44] C. Andeen, J. Fontanella, and D. Schuele, Phys. Rev. B **2**, 5068 (1970).

[45] As a matter of fact, h_d being very large, it can readily be verified that this result is always true whatever is the exact shape of the mesoscopic part of the tip apex.

[46] It must be noticed that the resonance frequency of that mode might be shifted owing to the influence of the overall attractive force, *i.e.* including Van der Waals, short-range and electrostatic components, similarly to the resonance frequency of the fundamental mode.

[47] In ref.[21], the foremost unstable atom of the tip which is responsible for the contrast in dissipation is triggerred at a distance of about 3 Å from the surface. Above that threshold, no instability is observed.

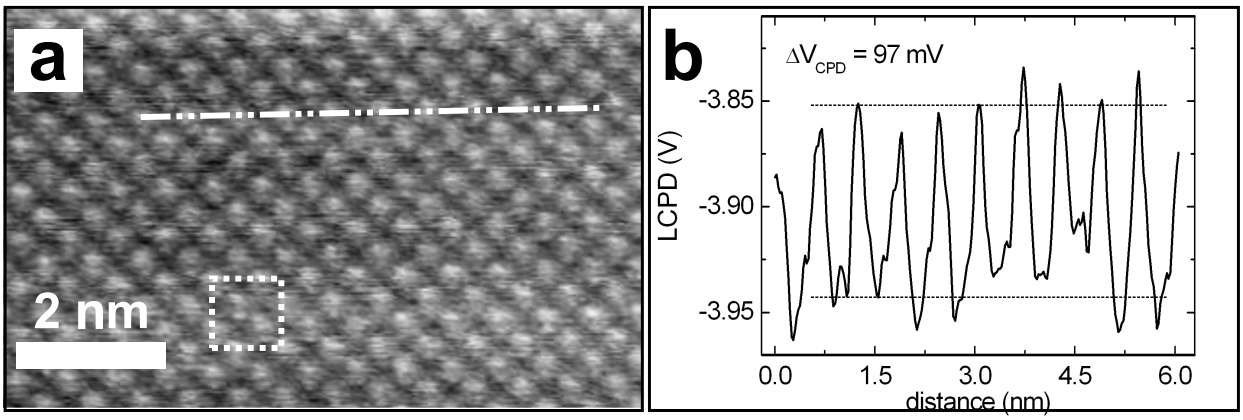

FIG. 1: a- Experimental image showing the atomic contrast of the compensated CPD measured on a (001) surface of KBr in ultra-high vacuum by means of AM-KPFM. The vertical contrast ranges from -3.95 to -3.85 V from dark to white spots. The dashed line depicts the cross section shown in b-. The dotted square depicts the area corresponding to the ball model shown in fig.2a. b- Corresponding cross section.

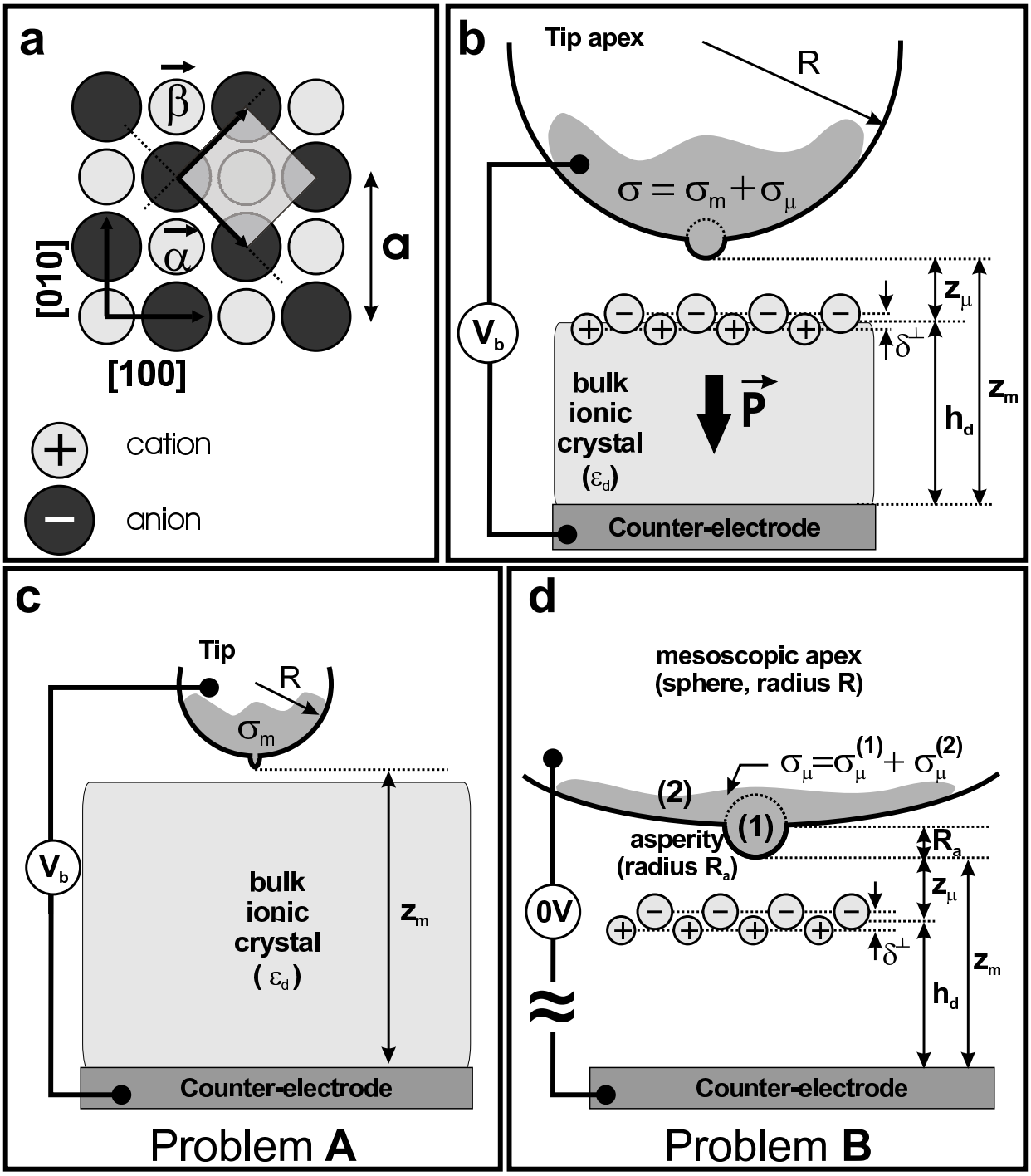

FIG. 2: a- KBr lattice with a fcc structure corresponding to the dotted square shown in fig.1a. The white spots of the experimental image have been placed on top of anions arbitrarily. b- Scheme of the KPFM experiment defining the electrostatic boundary-value problem to be solved. The metallic tip is biased with respect to a metallic counter-electrode placed a few millimeters far from it owing to the thickness of the ionic crystal. The bias voltage polarizes the crystal, which results, at the surface, in a modulation of the positions of the ions. c- and d- Schemes of the splitting of the original electrostatic boundary-value problem schemed in b- defining problems A and B.

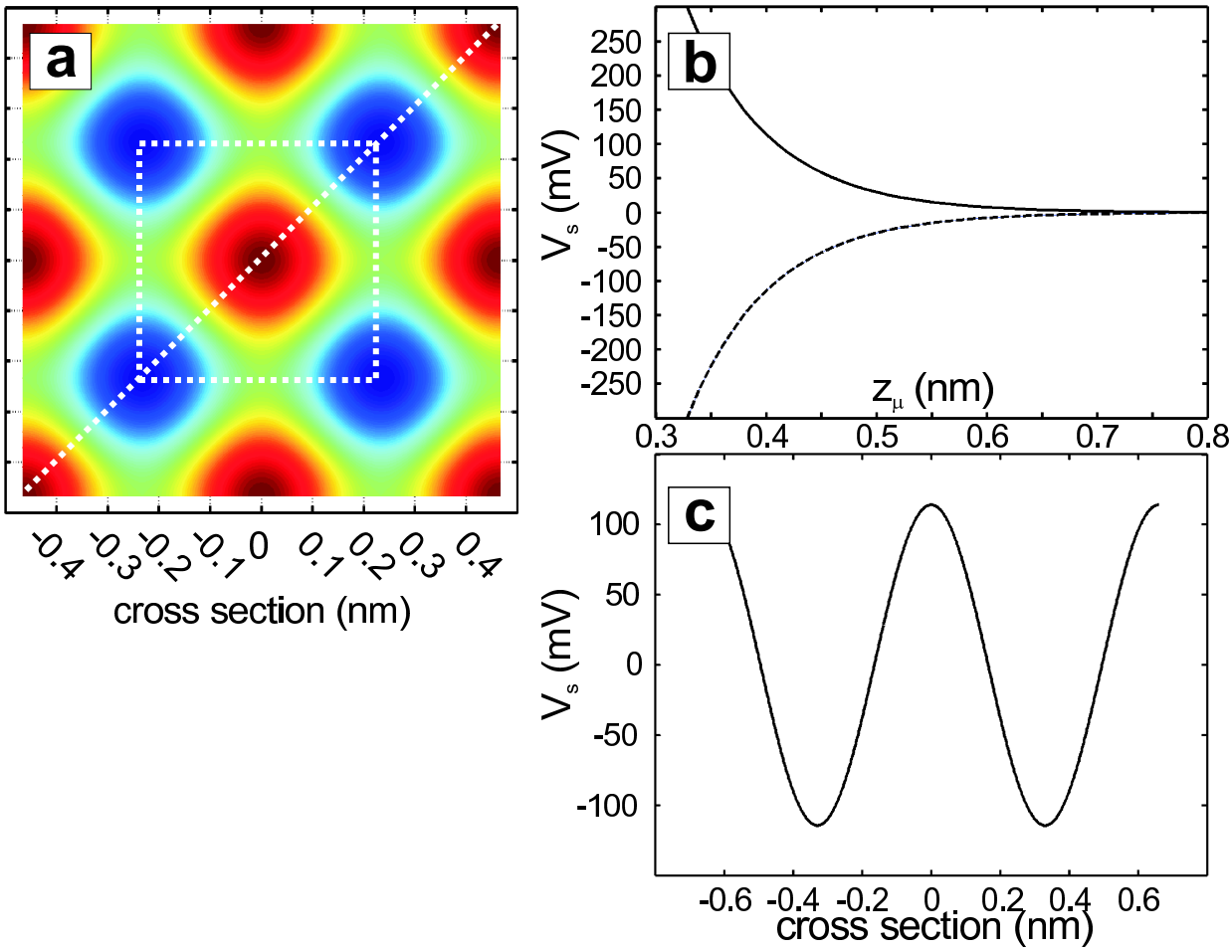

FIG. 3: (Color online). a- Madelung surface potential calculated from equ.14 for $a = 0.66$ nm, $\delta^{\perp} = 11$ pm and $z_{\mu} = 4$ Å. The vertical contrast ranges from -100 (blued spots) to $+100$ mV (reddish spots). The unit cell depicted with a dotted line is centered on a cation. b- Distance dependence of the potential on top of an anion (dotted curve) and on top of a cation (continuous curve) showing the exponential decay of the potential. c- Cross section along the dotted line shown in a-.

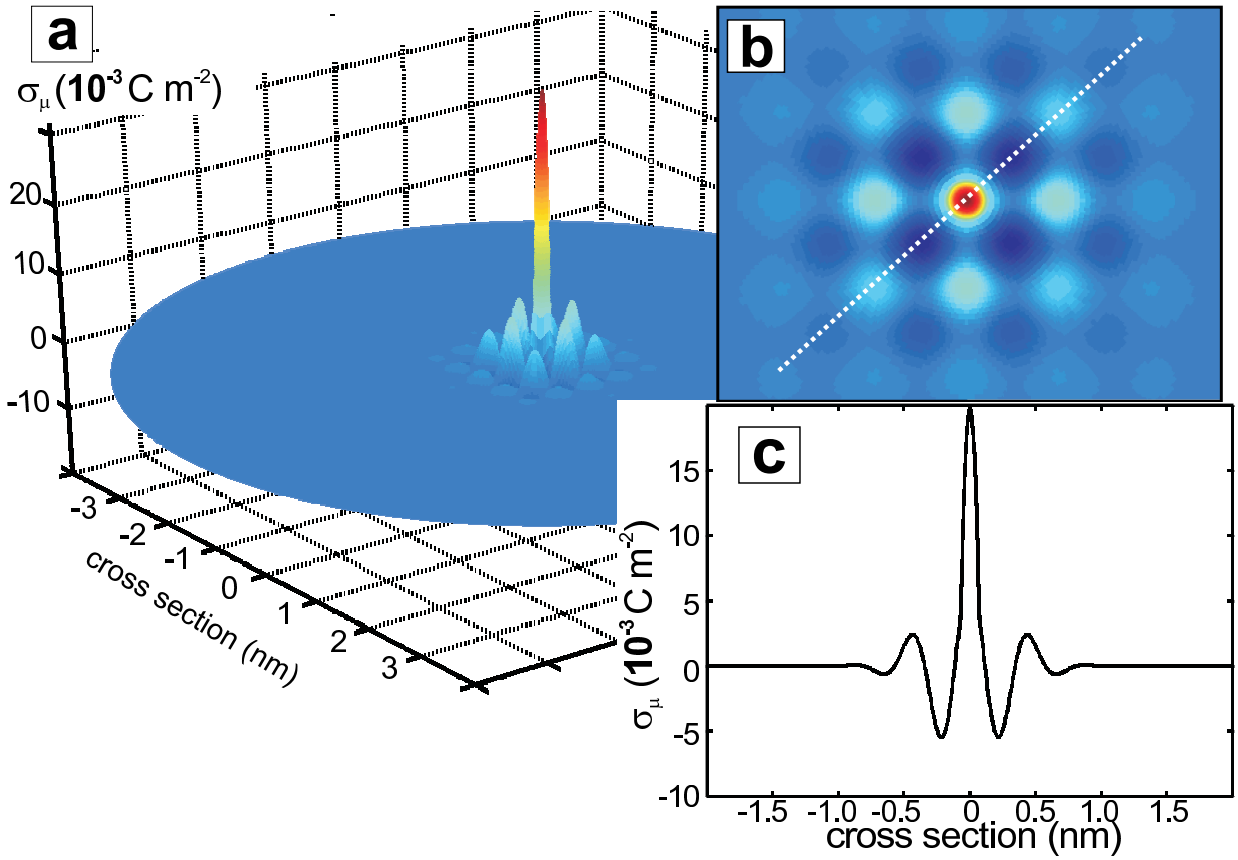

FIG. 4: (Color online) a- Perspective view of the projection of the microscopic surface charge density σ_μ on the tip calculated on top of an anion from equs.15 and 18 with $R_a = 1$ Å and $R = 5$ nm. σ_μ is strongly increased on top of the asperity. Then, owing to the exponential decay of the Madelung surface potential, the surface charge density strongly decreases, which makes the contribution of the mesoscopic apex weak. b- Top view of σ_μ. The oscillations due to the image charges of the ions at the surface of the crystal are well visible. The most part of the attenuation of σ_μ occurs within a single unit cell. Two unit cells apart from the asperity, σ_μ is almost zero. c-. Cross section along the dotted white line shown in b.

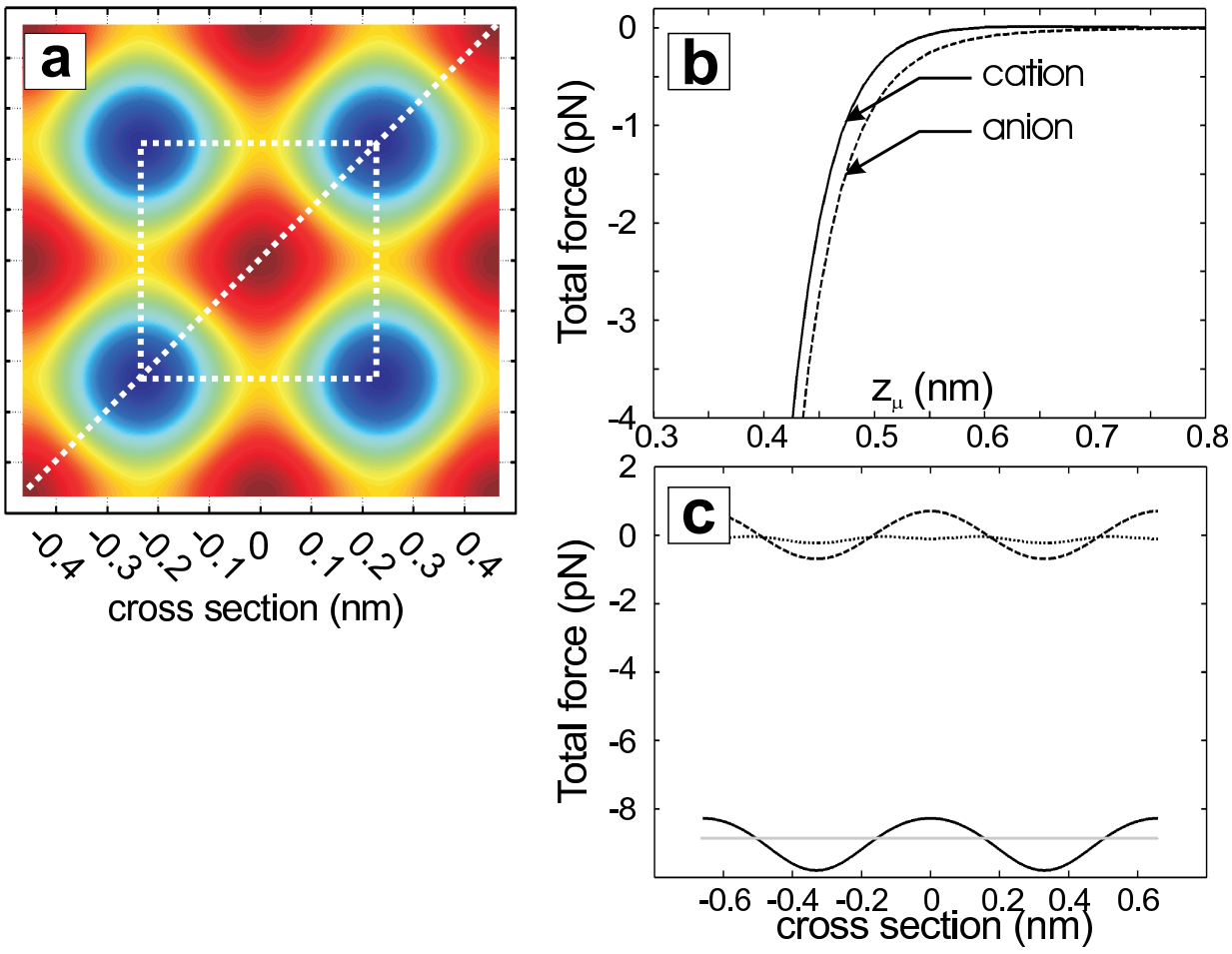

FIG. 5: (Color online). a- Total electrostatic force over a unit cell calculated from $F = F^{(1)}_{m\mu} + F^{(1)}_{\mu} + F^{(2)}_{\mu}$ for $a = 0.66$ nm, $\delta^{\perp} = 11$ pm, $z_{\mu} = 4$ Å and $V_b = +1$ V. The unit cell depicted with a dotted line is centered on a cation. The vertical contrast ranges from -10 (blued spots) to -8 pN (reddish spots). The force is more repulsive on top of cations (central ion) than on top of anions, consistently with the bias polarity. b- z_{μ} dependence of the electrostatic force on top of an anion (dotted curve) and on top of a cation (continuous curve). c- Cross section along the dotted line shown in a- showing the total force (thick continuous line), $F^{(1)}_{m\mu}$ (dashed line), $F^{(1)}_{\mu}$ (dotted line) and $F^{(2)}_{\mu}$ (greyed line). $F^{(1)}_{\mu}$ is negligible compared to the others.

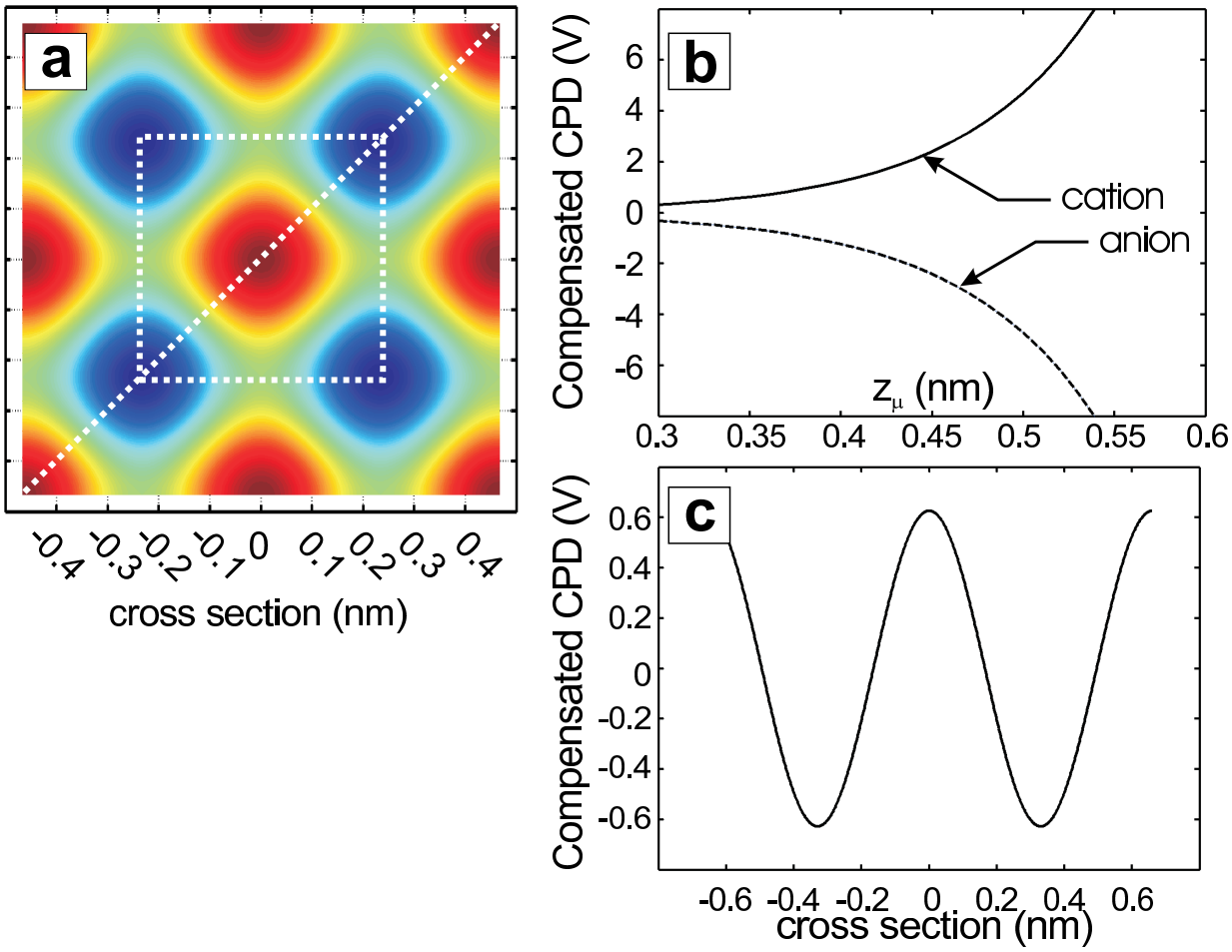

FIG. 6: (Color online). a- $V_{dc}^{(c)}$ bias voltage required to compensate the local CPD calculated from equ.45 for $a = 0.66$ nm, $\delta^{\perp} = 11$ pm, $A_0 = 5$ nm and $z_\mu = 3.5$ Å. The vertical contrast ranges from -0.6 (blued spots) to +0.6 V (reddish spots). The unit cell depicted with a dotted line is centered on a cation. b- Distance dependence of the potential on top of an anion (dashed curve) and on top of a cation (continuous curve). c- Cross section along the dotted line in a-.